

Article

Hierarchically Structured Graphene Aerogel Supported Nickel–Cobalt Oxide Nanowires as an Efficient Electrocatalyst for Oxygen Evolution Reaction

Donglei Guo ¹, Jiaqi Xu ¹, Guilong Liu ¹ and Xu Yu ^{2,*}

¹ Key Laboratory of Function-Oriented Porous Materials, College of Chemistry and Chemical Engineering, Luoyang Normal University, Luoyang 471934, China; gdl0594@163.com (D.G.); 18836032666@163.com (J.X.)

² Institute of Innovation Materials and Energy, School of Chemistry and Chemical Engineering, Yangzhou University, Yangzhou 225002, China

* Correspondence: yxypz15@yzu.edu.cn

Abstract: The rational design of a heterostructure electrocatalyst is an attractive strategy to produce hydrogen energy by electrochemical water splitting. Herein, we have constructed hierarchically structured architectures by immobilizing nickel–cobalt oxide nanowires on/beneath the surface of reduced graphene aerogels (NiCoO₂/rGAs) through solvent–thermal and activation treatments. The morphological structure of NiCoO₂/rGAs was characterized by microscopic analysis, and the porous structure not only accelerates the electrolyte ion diffusion but also prevents the agglomeration of NiCoO₂ nanowires, which is favorable to expose the large surface area and active sites. As further confirmed by the spectroscopic analysis, the tuned surface chemical state can boost the catalytic active sites to show the improved oxygen evolution reaction performance in alkaline electrolytes. Due to the synergistic effect of morphology and composition effect, NiCoO₂/rGAs show the overpotential of 258 mV at the current density of 10 mA cm^{−2}. Meanwhile, the small values of the Tafel slope and charge transfer resistance imply that NiCoO₂/rGAs own fast kinetic behavior during the OER test. The overlap of CV curves at the initial and 1001st cycles and almost no change in current density after the chronoamperometric (CA) test for 10 h confirm that NiCoO₂/rGAs own exceptional catalytic stability in a 1 M KOH electrolyte. This work provides a promising way to fabricate the hierarchically structured nanomaterials as efficient electrocatalysts for hydrogen production.

Keywords: hierarchical structure; nickel-cobalt oxide; graphene aerogel; oxygen evolution; transition metal nanowire



Citation: Guo, D.; Xu, J.; Liu, G.; Yu, X. Hierarchically Structured Graphene Aerogel Supported Nickel–Cobalt Oxide Nanowires as an Efficient Electrocatalyst for Oxygen Evolution Reaction. *Molecules* **2024**, *29*, 1805. <https://doi.org/10.3390/molecules29081805>

Academic Editor: Giuseppe Cirillo

Received: 6 April 2024

Revised: 14 April 2024

Accepted: 15 April 2024

Published: 16 April 2024



Copyright: © 2024 by the authors. Licensee MDPI, Basel, Switzerland. This article is an open access article distributed under the terms and conditions of the Creative Commons Attribution (CC BY) license (<https://creativecommons.org/licenses/by/4.0/>).

1. Introduction

Hydrogen energy with the merit of being a carbon-free product has become the focus of modern global attention and is considered the potential energy source to replace the consumption of transitional fossil fuels [1,2]. Hydrogen plays critical roles in both living organisms and various industrial processes, and the demand for hydrogen energy dramatically increased from 2000 (~59 Mt) to 2020 (~88 Mt), and is predicted to continue to rise by 2050 (~528 Mt) [3]. Electrochemical water splitting, including two half-reactions of the oxygen evolution reaction (OER) and hydrogen evolution reaction (HER), has attracted attention for producing hydrogen gas. Especially, the OER electrolysis is deemed to be a promising strategy for the formation of clean energy and energy conversion [4–6]. However, it is emergent to dissolve the issue of sluggish kinetics and complicated reactions during the OER process, which determines its faradic efficiency and requires a high overpotential to satisfy the practical applications [7]. The efficient electrocatalyst is the key factor in determining the catalytic reaction. The noble-metal-based electrocatalysts, such as iridium oxide (IrO₂) and ruthenium dioxide (RuO₂) [8–10], have been demonstrated to show outstanding OER activity, including low overpotential and high catalytic stability, but their high cost and

lack resources directly hinder their widespread application in commercialization. Based on these features, it is important to develop a cost-effective and naturally sustainable catalyst for the OER process.

Transition-metal-based nanostructures (Fe, Co, Ni, etc.) with earth-abundant resources, low prices, and abundant surface-active sites are favored by researchers, including transition metal oxides/hydroxides (TMOs) [11,12], transition metal sulfides (TMSs) [13,14], transition metal phosphides (TMPs) [15,16], transition metal fluorides (TMFs) [17,18], and transition metal nitrides (TMNs) [19], which have been generally evaluated as appreciable OER catalysts. Among them, TMO-based nanostructured catalysts have attracted attention owing to their exposed surface area and active sites, and their hybrids can show modified surface chemistry to boost the catalytic active sites for improved faradic efficiency and catalytic stability [20]. It has been proved that the reaction intermediates with the existence of covalent metal-O bonds can accelerate the catalytic reaction, and the adjusted strength of metal-O bonds is studied as the active site [11,21]. Numerous synthetic methods have been applied to construct the controllable morphology of catalysts, which extraordinarily affects catalytic efficiency, such as one-dimensional nanorods and nanowires [22–25]. Furthermore, the metallic atom-doped TMO catalysts with the bi-metallic alloying mechanism can result in surface reconstruction and adjust the electronic structure to improve electrocatalytic performance [26]. Moreover, the poor electrical conductivity of catalysts caused by the agglomeration of nanocomposites can be further tuned by introducing the conductive matrix into the catalysts.

Apart from the chemical compositional features, the controllable morphological structure is also important to determine the OER activity of the catalyst [27,28]. Carbon-based nanomaterial with high electronic conductivity is a promising candidate to accelerate the charge transfer during the OER process, while the controllable morphology of carbon-based materials can be obtained from different synthetic methods [29–32], such as hydrothermal, thermal annealing, etc. Graphene oxides, containing affluent surface functional groups (–OH and –COOH, etc.), can be easily modified to construct the hierarchical structure by the self-assembly of graphene nanosheets, and the unique porous structure can expose the large surface area and provide pathways for electrolyte ion facilitation [33,34]. Furthermore, the hybridization of carbon materials with TM components forms a strong TM/carbon interface [33,35–37], which can dramatically increase the electronic conductivity of the catalyst to guarantee the long-term durability of a catalyst during the OER process. Therefore, hybridizing NiCo₂ wires with hierarchical graphene aerogel as a cost-efficient catalyst for OER is an attractive strategy to satisfy the practical application of hydrogen production.

In this work, we have constructed the hierarchically structured electrocatalyst by hybridizing nickel–cobalt oxide nanowires with reduced graphene aerogels (NiCoO₂/rGAs) through a facial hydrothermal method. The hierarchical structure remained after freeze-drying treatment, which is beneficial for providing a large surface area and increasing the utilization of active sites. The surface chemistry is tuned, and the surface-active sites are boosted by the strong electrochemical interaction at the NiCoO₂/graphene interface. Due to the synergistic effect of high porosity and modified surface chemical states, NiCoO₂/rGAs exhibit exceptional catalytic OER performance. To afford the current density of 10 mA cm^{−2}, the overpotential of NiCoO₂/rGAs is smaller with the lower Tafel slope and smaller charge transfer resistance than the control catalysts, implying a fast kinetic behavior for NiCoO₂/rGAs. No apparent change in current density confirms good catalytic stability of NiCoO₂/rGAs.

2. Results and Discussion

2.1. Morphological Structure of NiCoO₂/rGAs

A schematic illustration of the synthetic process of NiCoO₂/rGAs is shown in Figure 1a, and the hierarchically structured catalysts are prepared through the hydrothermal method and low-temperature activation treatment. The quality of the mixture is crucial to prepare the hierarchically structured aerogel. Firstly, the nickel chlorides, cobalt chlorides, and

graphene are mixed to obtain a uniform distribution and are treated via a facile hydrothermal method to initially obtain the metal-ion functionalized graphene hydrogel. During the hydrothermal process, graphene oxides with abundant surface functional groups ($-\text{OH}$, $-\text{COOH}$, etc.) are self-assembled by forming the π - π bonding configuration and hydrogen bonds, and the hierarchical structure of graphene hydrogel is constructed by the crosslink of graphene oxide nanosheets. Subsequently, the hydrogel was mixed with oxalic acid in ultrapure water, and the nanowires were grown on or beneath the surface of graphene, which is helpful to avoid the agglomeration of nanowires. After the freeze-drying treatment for 3 days, the aerogel with hierarchical structure is kept, which is further heated at $400\text{ }^\circ\text{C}$ under a nitrogen atmosphere to finally obtain the $\text{NiCoO}_2/\text{rGAs}$ catalyst.

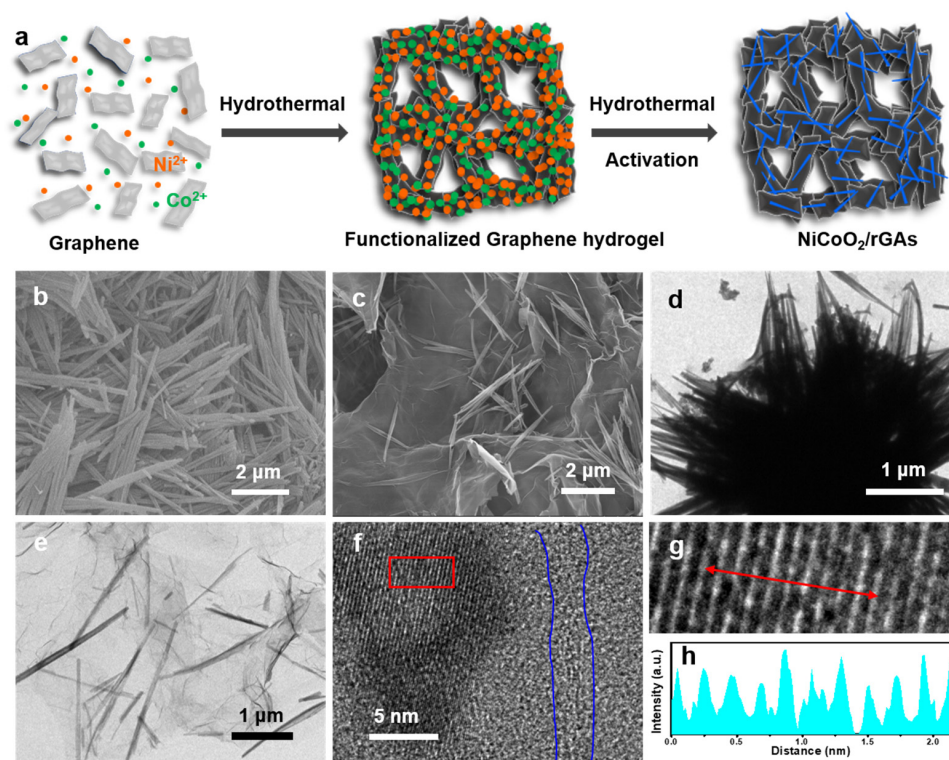


Figure 1. (a) Schematic illustration of the preparation of $\text{NiCoO}_2/\text{rGAs}$. SEM images of (b) NiCoO_2 and (c) $\text{NiCoO}_2/\text{rGAs}$. TEM images of (d) NiCoO_2 and (e) $\text{NiCoO}_2/\text{rGAs}$. (f,g) High-resolution TEM images of $\text{NiCoO}_2/\text{rGAs}$. (h) The measured lattice spacing of NiCoO_2 in $\text{NiCoO}_2/\text{rGAs}$ (a profile of (g)).

The morphological structure of $\text{NiCoO}_2/\text{rGAs}$ was initially probed by a scanning electron microscope (SEM). Figure 1b shows the morphology of NiCoO_2 nanowires, and an apparent agglomeration of nanowires can be observed. After incorporating graphene aerogels during the hydrothermal and activation process, $\text{NiCoO}_2/\text{rGAs}$ show the hierarchical structure in Figure 1c, which is composed of graphene nanosheets and NiCoO_2 nanowires. Meanwhile, the NiCoO_2 nanowires distribute on/beneath the surface of graphene without severe agglomeration, which arises from the supporter of graphene aerogel. The merit of unique morphology is beneficial to provide channels for fast electrolyte diffusion, expose the effective active sites, and increase their utilization. The transmission electron microscopy (TEM) technique was further characterized to evaluate the morphology of $\text{NiCoO}_2/\text{rGAs}$. As shown in Figure 1d, the aggregated NiCoO_2 nanowires are observed. Figure 1e shows the TEM image of $\text{NiCoO}_2/\text{rGAs}$. The transparent graphene nanosheets of $\text{NiCoO}_2/\text{rGAs}$ can be observed, and NiCoO_2 nanowires are distributed on the surface of graphene without agglomeration, which agrees with the SEM analysis. The high-resolution TEM images are shown in Figure 1f,g, and Figure 1h is an enlargement of the selected region in Figure 1f. $\text{NiCoO}_2/\text{rGAs}$ show an apparent lattice fringe with a d-spacing of

0.21 nm, corresponding to the (200) plane of NiCoO₂ in Figure 1h [38]. Meanwhile, the region marked in blue is ascribed to graphene oxides.

The high porosity of NiCoO₂/rGAs was evaluated by the nitrogen adsorption/desorption isotherms in Figure 2a, and the specific surface area is 121.5 m² g⁻¹ with an average pore size of 14.3 nm. The large specific surface area is beneficial to increase the contact between the catalyst and electrolyte and expose the boosted active sites on the surface of the catalyst. To verify the crystallinity of NiCoO₂/rGAs, an X-ray diffraction technique was carried out in Figure 2b. The diffraction peak for rGAs centering at 25.3° is indexed to the typical (002) pattern of graphite carbon, implying that the unstable surface functional groups on the surface of graphene are reduced [39]. In comparison to rGAs, NiCoO₂/rGAs show a weak diffraction peak at 25.3° corresponding to the (002) plane of graphite carbon, and the slight shift of (002) peaks can be assigned to the expanded distance by forming the NiCoO₂/graphene interface. Meanwhile, other XRD patterns of NiCoO₂/rGAs are consistent with the standard NiCoO₂ [PDF #10-0188], and three primary diffraction peaks indexed at 36.7°, 42.7°, and 61.8° are evident for the NiCoO₂/rGAs and are assigned to the typical (111), (200), and (220) planes, respectively. The XRD analysis confirms that NiCoO₂/rGAs consist of crystal NiCoO₂ and graphene.

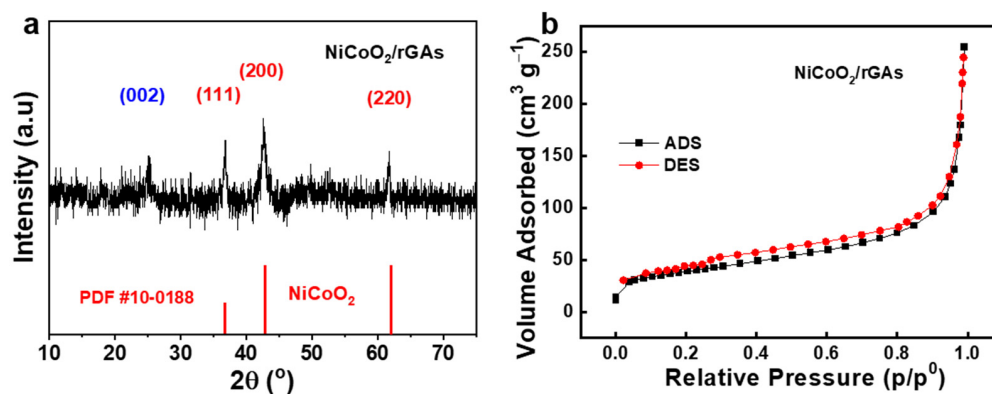


Figure 2. (a) XRD spectra and (b) nitrogen adsorption/desorption isotherms of NiCoO₂/rGAs.

To evaluate the surface environment of the NiCoO₂/rGA catalyst, X-ray photoelectron spectroscopy (XPS) was carried out, and all the spectra were calibrated by C 1 s peaks at 284.6 eV. As shown in Figure 3a, the full scan XPS spectra show four primary peaks corresponding to the C, O, Co, and Ni elements, and the strong peak of the oxygen element may primarily come from the formation of bi-metallic oxides by decomposing the synthesized metal compounds and the adsorbed water during the sample preparation process. Figure 3b shows the high-resolution C 1 s spectra of NiCoO₂/rGAs, and the deconvoluted peaks at 284.6, 285.3, and 285.9 eV are attributed to the C-C, C-O, and C=O bonds [29]. For the high-resolution Ni 2 p spectra in Figure 3c, two primary peaks at the binding energy of 853.5 and 870.9 eV correspond to the spin orbital of Ni 2 p_{3/2} and Ni 2 p_{1/2}, accompanied by the related satellite peaks at 859.6 and 877.2 eV, respectively [40]. Meanwhile, the Ni 2 p_{3/2} can be rationally divided into two peaks at 852.6 and 854.7 eV owing to the Ni²⁺ and the multiple splitting of Ni³⁺, and two fitted peaks for Ni 2 p_{1/2} at 870.5 and 873.2 eV correspond to Ni²⁺ and of Ni³⁺, implying the presence of divalent oxidized species of Ni in NiCoO₂/rGAs. The core-level spectra of Co 2 p are shown in Figure 3d, which consist of the two spin orbital doublets and the related shakeup satellite peaks. Four easily discernible peaks in Co 2 p can be fitted, including the major peak of Co 2 p_{3/2} with the related satellite peak and the primary peak of Co 2 p_{1/2} with the related satellite peak, respectively [41]. The peaks centered at 782.5 and 798.9 eV are attributed to the Co 2 p_{3/2} and Co 2 p_{1/2} accompanied by their satellite peaks at 788.6 and 804.8 eV. The energy gap between Co 2 p and its shakeup satellite peak is about 4.8 eV for Co²⁺ and 6.4 eV for Co³⁺, indicating the existence of the divalent oxidized state of Co

species in NiCoO₂/rGAs. For the high-resolution O 1s peak in Figure 3e, the peak can be deconvoluted into two primary oxygen contributions. The peak centered at 532.6 eV corresponds to the typical metal-O bond [42], and the other peak centered at 535.8 eV is ascribed to the C-O/C=O bond of surface oxidized carbon species. As confirmed by the above XPS analysis, NiCoO₂/rGAs include the metallic Co and Ni ions and C and O elements. The atomic ratios of Ni and Co elements are 5.85% and 6.03%, which are matched with the stoichiometry ratio of NiCoO₂.

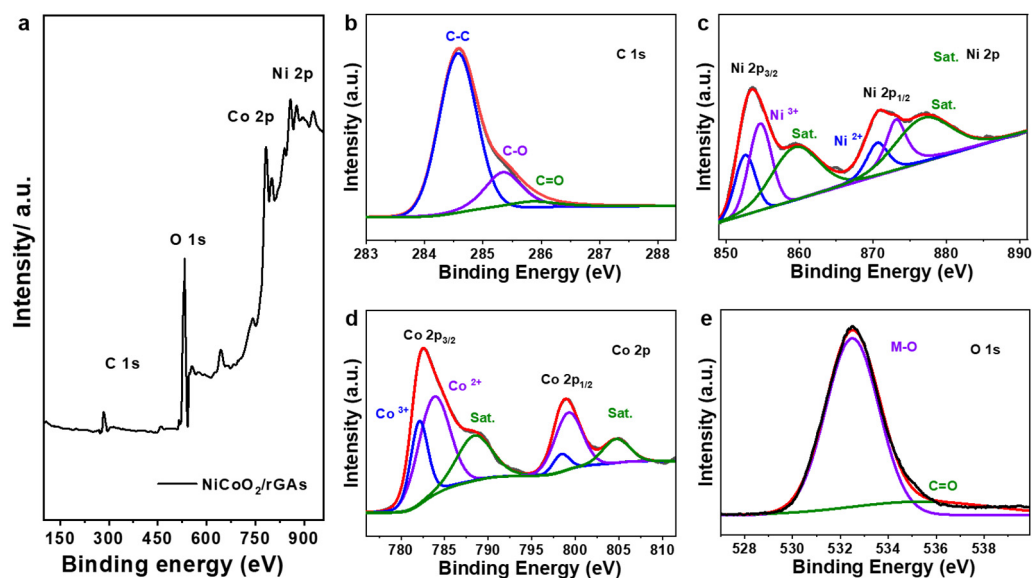


Figure 3. (a) Full survey XPS spectra and high-resolution (b) C 1s, (c) Ni 2p, (d) Co 2p, and (e) O 1s spectra of NiCoO₂/rGAs.

2.2. Electrocatalytic OER Performance

To evaluate the electrochemical OER activity of NiCoO₂/rGAs, a cyclic voltammetry (CV) test was applied through a typical three-electrode system, and 1 M KOH as the electrolyte was pretreated by constant flow of N₂. After the activation of the catalyst, the polarization curve of NiCoO₂/rGAs was measured at a scan rate of 5 mV s⁻¹, and the control sample of NiCoO₂ and rGAs catalysts was measured under identical conditions as the comparison. It is worth noting that all the potentials of catalysts have been calculated after IR correction. During the OER measurement, the NiCoO₂/rGAs catalyst acts as the working electrode, and the graphitic carbon and saturated calomel electrode act as the counter and reference electrodes. The polarization curves of all catalysts at 5 mV s⁻¹ are shown in Figure 4a, and NiCoO₂/rGAs have an overpotential of 258 mV to afford a current density of 10 mA cm⁻², which is more negative than that of NiCoO₂ (275 mV) and rGAs (332 mV). Specifically, the overpotentials for NiCoO₂/rGAs are 280 mV at the current density of 20 mA cm⁻² and 321 mV at the current density of 50 mA cm⁻², which are both lower than those of NiCoO₂ (300 mV at 20 mA cm⁻² and 355 at 50 mA cm⁻²) and rGAs (372 mV at 20 mA cm⁻²) in Figure 4b, unveiling that the NiCoO₂/rGA as the non-noble-metal catalyst owns exceptional OER activity. Tafel slope is a crucial parameter to reflect the obstructive condition of the electrode during the reaction process, which can be obtained by the formula $\eta = a + b \log(j)$, where *a* and *b* are the constant values, η is the overpotential (mV), and *j* is the current density (mA cm⁻²). It is well known that *a* represents the overpotential when the current density is a unit value (1 A cm⁻²), which is strongly related to the intrinsic property and the surface chemical state of electrode materials [43], etc. The values of the Tafel slope are compared to evaluate the catalytic kinetics and calculated from their polarization curves. The values of Tafel slope are 68, 77, and 132 mV dec⁻¹ for NiCoO₂/rGAs, NiCoO₂, and rGAs in Figure 4c. A smaller Tafel slope for NiCoO₂/rGAs elucidates a faster kinetic property and better catalytic OER

activity than other control samples. As reported by lectures, a Tafel slope with values of 30, 40, and 120 mV dec^{-1} represents the Volmer process, the Volmer–Heyrovsky process, and the Heyrovsky process, which are the major rate-determining steps during the OER process [44]. $\text{NiCoO}_2/\text{rGAs}$ with a value of 68 mV dec^{-1} imply that the Volmer–Heyrovsky process is the dominant rate-determining step.

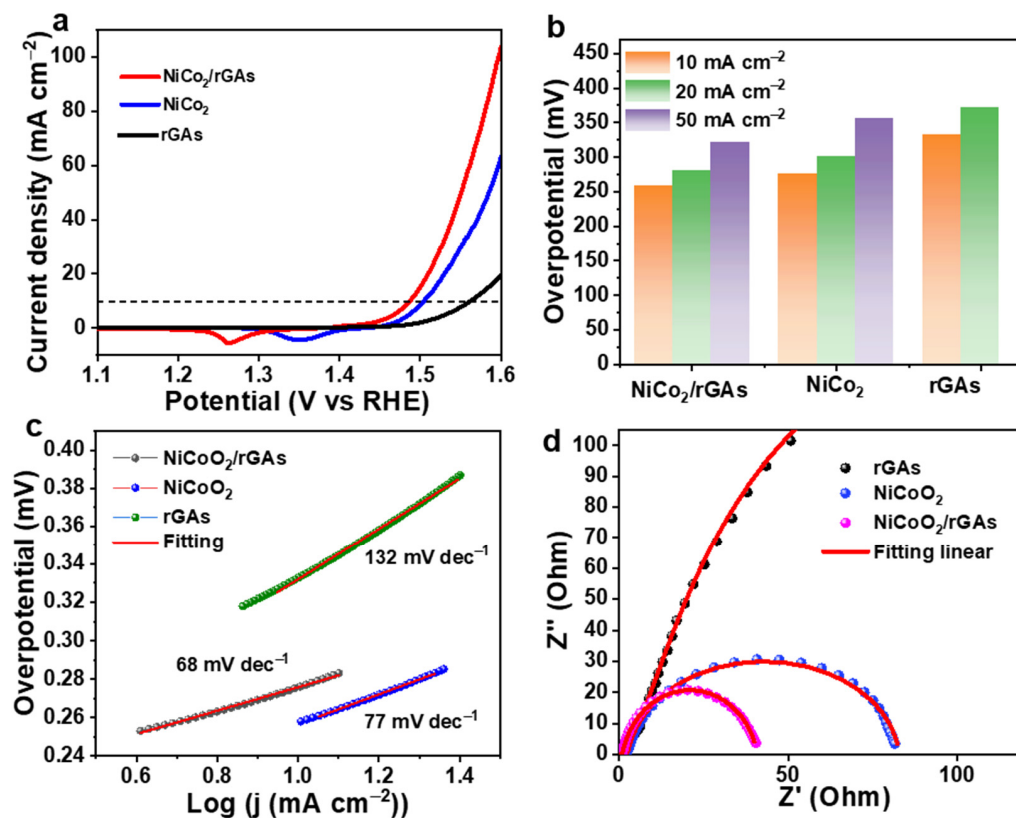


Figure 4. (a) Polarization curves at 5 mV s^{-1} in 1 M KOH , (b) the overpotentials at different current densities, (c) Tafel slopes, and (d) Nyquist plots of NiCo_2 , rGAs and $\text{NiCo}_2/\text{rGAs}$.

The dynamic property of $\text{NiCo}_2/\text{rGAs}$ was further investigated by electrochemical impedance spectroscopy (EIS) in Figure 4d. The electrical equivalent circuit applied to deconvolute the Nyquist plots includes the parameters R_1 , R_s , and R_{ct} , which are the reflections of solution resistance, contact resistance between electrode and electrolyte, and charge transfer resistance (inset of Figure 4d) [45]. At high frequency, the R_{ct} value of $\text{NiCo}_2/\text{rGAs}$ is lower than that of NiCo_2 and rGAs with a semicircle with a smaller diameter, elucidating a fast charge transfer and exceptional OER activity for $\text{NiCo}_2/\text{rGAs}$ during the OER process. The smallest Tafel slopes and R_{ct} values of $\text{NiCo}_2/\text{rGAs}$ can be attributed to the introduction of graphene aerogel into the NiCo_2 system, and the electronic conductivity of $\text{NiCo}_2/\text{rGAs}$ is dramatically increased, which can strongly guarantee the good electrocatalytic OER performance in an alkaline electrolyte.

$\text{NiCo}_2/\text{rGAs}$ with a hierarchical structure can provide a large specific surface area and expose abundant active sites, which are favorable for improving electrocatalytic OER performance. To unveil the effect of hierarchical morphology on the catalytic OER performance, the double layer capacitance (C_{dl}) was obtained by integrating the specific current density of CV curves. The CV curves of all the catalysts were tested at a series of scan rates from 5 mV s^{-1} to 50 mV s^{-1} (Figure 5a–c), and the calculated C_{dl} values for all catalysts are shown in Figure 5d. The C_{dl} value of $\text{NiCo}_2/\text{rGAs}$ is 9.02 mF cm^{-2} , which is about 1.7 and 3.0 times higher than that of NiCo_2 (5.28 mF cm^{-2}) and rGAs (3.03 mF cm^{-2}), implying a larger specific area and exposed active sites of $\text{NiCo}_2/\text{rGAs}$. The hierarchically structured graphene aerogel not only provides channels for fast ion diffusion but also

inhibits the agglomeration of NiCoO₂ nanowires and exposes the active sites for the OER test. To satisfy the practical application in hydrogen production, the long-term durability of the catalyst as a crucial factor was initially confirmed by CV curves for 1000 cycles at 5 mV s⁻¹. In comparison to its initial cycle, the CV curve at the 1001st cycle is almost overlapped, and the overpotential is slightly increased with the value of 3 mV (Figure 5e), demonstrating that NiCoO₂/rGAs owns good electrocatalytic OER durability. As further confirmed by chronoamperometry (CA) measurement at an overpotential of 258 mV for 10 h (Figure 5f), the current density has almost no loss during the sustaining operation. The CV curve for 1000 cycles and the CA test for 10 h strongly demonstrate the outstanding electrocatalytic OER stability in an alkaline electrolyte.

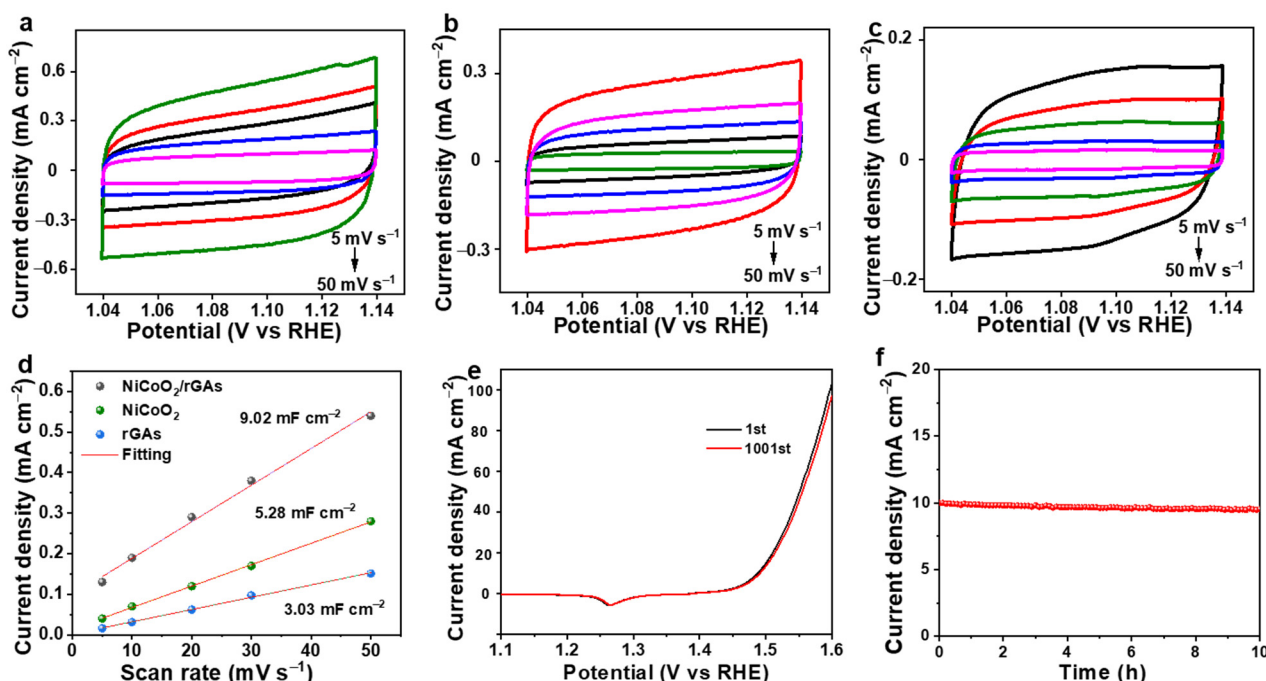


Figure 5. CV curves of (a) NiCoO₂/rGAs, (b) NiCoO₂, and (c) rGAs. (d) Cdl values of NiCoO₂, rGAs and NiCoO₂/rGAs. (e) CV curves at the 1st and 1001st cycles and (f) the CA test for 10 h of NiCoO₂/rGAs.

Due to the synergistic effect of the controllable morphological structure and composition, NiCoO₂/rGAs can show exceptional OER performance in an alkaline electrolyte, and the detailed possibilities are listed below. (1) The hierarchical structure constructed from the self-assembly of graphene nanosheets can expose the large surface area and more active sites, accelerate the ion diffusion in the channels, and prevent the agglomeration of NiCoO₂ nanowires. (2) The NiCoO₂ nanowires with uniform morphology can deposit on or beneath graphene and act as the dominant active sites. (3) The strong chemical coupling between NiCoO₂ and graphene can tune the surface chemical environment and boost the catalytic sites for the significant enhancement of OER performance.

3. Materials and Methods

3.1. Preparation of NiCoO₂

A total of 10 mL of ultrapure water and 25 mL of ethylene glycol were mixed in a 100 mL glass beaker (100 mL) and then mixed with 150 mg of NiCl₂·6H₂O and 150 mg of CoCl₂ under magnetic stirring for 20 min. Subsequently, 150 mg of oxalic acid was added into the beaker and stirred for 20 min. The dispersion was transferred to the stainless-steel autoclave (100 mL) and then the autoclave was heated at 180 °C for 10 h. The precipitation was washed with ethanol/deionized water several times and dried at

60 °C in a vacuum atmosphere. The powder was further annealed at 350 °C for 1 h under a nitrogen atmosphere with a heat rate of 10 °C min⁻¹ and a gas flow rate of 100 cc min⁻¹. The finally obtained sample was noted as NiCoO₂ nanowires.

3.2. Preparation of rGAs

A total of 15 mL of graphene oxides (6 mg mL⁻¹) were dispersed in 35 mL of ultrapure water under magnetic stirring for 20 min. The final dispersion was poured into a 100 mL stainless-steel autoclave and heated at 180 °C for 10 h. The hydrogel was washed by the solvent of ethanol/deionized water several times and solidified in liquid nitrogen. The hydrogel was freeze-dried for 3 days. The black aerogel was placed in the tube furnace and further annealed at 350 °C for 1 h at vacuum conditions. The sample was finally obtained and noted as rGAs.

3.3. Preparation of NiCoO₂/rGAs

A mixture of ultrapure water (10 mL) and ethylene glycol (25 mL) was prepared in a glass beaker (100 mL) and worked as the solvent. A total of 150 mg of NiCl₂·6H₂O, 150 mg of CoCl₂, and 15 mL of graphene oxide dispersion (6 mg mL⁻¹) were dispersed in the solvent under magnetic stirring for 20 min. Subsequently, 150 mg of oxalic acid was added into the beaker drop by drop with continuous magnetic stirring for 20 min to obtain the homogeneous dispersion. The final dispersion was poured into a 100 mL stainless-steel autoclave, and then the autoclave was heated at 180 °C for 10 h. The hydrogel was washed with the solvent of ethanol/deionized water several times and then immersed in liquid nitrogen until all the solvent was solidified. The solidified hydrogel was treated by freeze-drying for 3 days. The black aerogel was placed in the tube furnace and further annealed at 350 °C for 1 h at vacuum conditions. The heat rate is 10 °C min⁻¹ and the flow rate of nitrogen gas is 100 cc min⁻¹. The finally obtained sample was noted as NiCoO₂/rGAs.

3.4. Characterization

The crystallinity of the catalyst was characterized by powder X-ray diffraction (XRD) (Bruker D8 Advance powder X-ray diffractometer, Cu K α , λ = 1.5405 Å, 40 kV, Bruker, Billerica, MA, USA). Scanning electron microscopy (FESEM, Hitachi, S-4800 II, Tokyo, Japan) and transmission electron microscopy (TEM, Philips, TECNAI 12, Amsterdam, The Netherlands) were applied to evaluate the morphology. All X-ray photoelectron spectroscopy (XPS) measurements were probed to confirm the surface chemical state (Kratos XSAM-800 spectrometers, Al K α radiation source, Manchester, UK).

3.5. Electrochemical Measurements

The electrochemical experiments were conducted using a DH7000C electrochemical workstation (Donghua Test, Taizhou, China) in a standard three-electrode configuration. The catalyst ink was prepared by mixing 5 mg of catalyst with 950 μ L of ethanol and 50 μ L of Nafion, followed by sonication for 30 min. The reference and counter electrodes consisted of a saturated calomel electrode (SCE) and a graphite rod, respectively. A glassy carbon electrode (GCE) was employed as the working electrode, and 10 μ L of the catalyst ink was drop-cast and air-dried to achieve a loading of 0.71 mg cm⁻². The potentials were calculated using the equation $E(\text{RHE}) = E(\text{SCE}) + 0.0591 \times \text{pH} + 0.242 \text{ V}$, with RHE representing the reversible hydrogen electrode.

Cyclic voltammetry (CV) measurements were performed across a range of current densities from 5 to 50 mV s⁻¹, while the catalytic stability was evaluated through a chronoamperometry (CA) test conducted over a 10 h period. The kinetic properties of the catalyst were investigated using electrochemical impedance spectroscopy (EIS) over a frequency range from 100 kHz to 10 Hz. Additionally, CV curves were acquired in the non-faradic region at scan rates ranging from 5 to 50 mV s⁻¹.

4. Conclusions

In summary, the hierarchically structured catalyst by coupling NiCoO₂ nanowires with reduced graphene oxide aerogels was synthesized via a facile hydrothermal method and activation approach. As confirmed by microscopic analysis, the distribution of NiCoO₂ nanowires on the surface of graphene is uniform, and the hierarchical structure of the catalyst can facilitate electrolyte diffusion and expose a large surface area. The surface chemistry of the catalyst is caused by the hybridization of nanowires with graphene, and the formation of an interface can boost the catalytic active sites. According to the specific morphology and tuned surface environment, NiCoO₂/rGAs show outstanding OER performance, such as low overpotential, small Tafel slope and charge transfer resistance, and good catalytic durability. This study provides a straightforward methodology for fabricating hierarchically structured nanocomposites as efficient electrocatalysis for oxygen evolution reactions.

Author Contributions: Formal analysis, conceptualization, funding acquisition, writing—original draft, and investigation, D.G.; investigation, G.L.; methodology, resources, and investigation, J.X.; supervision, writing—review and editing, and resources, X.Y. All authors have read and agreed to the published version of the manuscript.

Funding: This research was funded by the Key Science and Technology Program of Henan Province (Grant number 222102240044); the Natural Science Foundations of Henan Province [Grant number 242300420045], the Program for Science and Technology Innovation Talents in Universities of Henan Province [Grant number 24HASTIT006], and the ‘High-End Talent Project’ of Yangzhou University.

Institutional Review Board Statement: Not applicable.

Informed Consent Statement: Not applicable.

Data Availability Statement: Data are contained within the article.

Acknowledgments: We acknowledge the technical support from the Testing Center of Yangzhou University. The authors would like to thank the anonymous reviewers who helped to significantly improve the quality of the research article.

Conflicts of Interest: The authors declare no conflicts of interest.

References

1. Qiu, Z.; Li, Y.; Gao, Y.; Meng, Z.; Sun, Y.; Bai, Y.; Suen, N.-T.; Chen, H.-C.; Pi, Y.; Pang, H. 2D MOF-assisted Pyrolysis-displacement-alloying Synthesis of High-entropy Alloy Nanoparticles Library for Efficient Electrocatalytic Hydrogen Oxidation. *Angew. Chem. Int. Ed.* **2023**, *62*, e202306881. [[CrossRef](#)] [[PubMed](#)]
2. Pi, Y.; Qiu, Z.; Sun, Y.; Ishii, H.; Liao, Y.-F.; Zhang, X.; Chen, H.-Y.; Pang, H. Synergistic Mechanism of Sub-Nanometric Ru Clusters Anchored on Tungsten Oxide Nanowires for High-Efficient Bifunctional Hydrogen Electrocatalysis. *Adv. Sci.* **2023**, *10*, 2206096. [[CrossRef](#)] [[PubMed](#)]
3. Guan, D.; Wang, B.; Zhang, J.; Shi, R.; Jiao, K.; Li, L.; Wang, Y.; Xie, B.; Zhang, Q.; Yu, J.; et al. Hydrogen society: From present to future. *Energy Environ. Sci.* **2023**, *16*, 4926–4943. [[CrossRef](#)]
4. Wang, J.; Yang, G.; Jiao, Y.; Yan, H.; Fu, H. Subtle 2D/2D MXene-Based Heterostructures for High-Performance Electrocatalytic Water Splitting. *Small Methods* **2024**, 2301602. [[CrossRef](#)] [[PubMed](#)]
5. Liang, J.; Li, S.; Li, F.; Zhang, L.; Jiang, Y.; Ma, H.; Cheng, K.; Qing, L. Defect engineering induces Mo-regulated Co₉Se₈/FeNiSe heterostructures with selenium vacancy for enhanced electrocatalytic overall water splitting in alkaline. *J. Colloid Interface Sci.* **2024**, *655*, 296–306. [[CrossRef](#)] [[PubMed](#)]
6. Huang, X.; Yu, L.; Wang, X.; Feng, L. Insights into Fe-doping effect-induced heterostructure formation for the oxygen evolution reaction. *Chem. Commun.* **2023**, *59*, 12294–12297. [[CrossRef](#)] [[PubMed](#)]
7. Huang, J.; Li, P.; Chen, S. Quantitative Understanding of the Sluggish Kinetics of Hydrogen Reactions in Alkaline Media Based on a Microscopic Hamiltonian Model for the Volmer Step. *J. Phys. Chem. C* **2019**, *123*, 17325–17334. [[CrossRef](#)]
8. Lee, Y.; Suntivich, J.; May, K.J.; Perry, E.E.; Shao-Horn, Y. Synthesis and Activities of Rutile IrO₂ and RuO₂ Nanoparticles for Oxygen Evolution in Acid and Alkaline Solutions. *J. Phys. Chem. Lett.* **2012**, *3*, 399–404. [[CrossRef](#)] [[PubMed](#)]
9. Qin, Y.; Yu, T.; Deng, S.; Zhou, X.-Y.; Lin, D.; Zhang, Q.; Jin, Z.; Zhang, D.; He, Y.-B.; Qiu, H.-J.; et al. RuO₂ electronic structure and lattice strain dual engineering for enhanced acidic oxygen evolution reaction performance. *Nat. Commun.* **2022**, *13*, 3784. [[CrossRef](#)]

10. Xu, J.; Yu, L.; Dong, B.; Yang, F.; Feng, L. Ruthenium-nickel oxide derived from Ru-coupled Ni metal–organic framework for effective oxygen evolution reaction. *J. Colloid Interface Sci.* **2024**, *654*, 1080–1088. [[CrossRef](#)]
11. Song, F.; Bai, L.; Moysiadou, A.; Lee, S.; Hu, C.; Liardet, L.; Hu, X. Transition Metal Oxides as Electrocatalysts for the Oxygen Evolution Reaction in Alkaline Solutions: An Application-Inspired Renaissance. *J. Am. Chem. Soc.* **2018**, *140*, 7748–7759. [[CrossRef](#)] [[PubMed](#)]
12. Hu, J.; Li, Z.; Zhao, D.; Han, Z.; Wu, X.; Zhai, J.; Liu, Z.; Tang, Y.; Fu, G. l-Lysine-induced green synthesis of CoS/Co₃O₄ nanoframes for efficient electrocatalytic oxygen evolution. *Green Chem.* **2023**, *25*, 7309–7317. [[CrossRef](#)]
13. Wang, M.; Zhang, L.; He, Y.; Zhu, H. Recent advances in transition-metal-sulfide-based bifunctional electrocatalysts for overall water splitting. *J. Mater. Chem. A* **2021**, *9*, 5320–5363. [[CrossRef](#)]
14. Guo, Y.; Jia, K.; Dai, F.; Liu, Y.; Zhang, C.; Su, J.; Wang, K. Hierarchical porous tri-metallic NiCoFe-Se/CFP derived from Ni-Co-Fe Prussian blue analogues as efficient electrocatalyst for oxygen evolution reaction. *J. Colloid Interface Sci.* **2023**, *642*, 638–647. [[CrossRef](#)] [[PubMed](#)]
15. Xu, J.; Li, J.; Xiong, D.; Zhang, B.; Liu, Y.; Wu, K.-H.; Amorim, I.; Li, W.; Liu, L. Trends in activity for the oxygen evolution reaction on transition metal (M = Fe, Co, Ni) phosphide pre-catalysts. *Chem. Sci.* **2018**, *9*, 3470–3476. [[CrossRef](#)] [[PubMed](#)]
16. Wei, Y.; Zheng, M.; Zhu, W.; Zhang, Y.; Hu, W.; Pang, H. Preparation of hierarchical hollow CoFe Prussian blue analogues and its heat-treatment derivatives for the electrocatalyst of oxygen evolution reaction. *J. Colloid Interface Sci.* **2023**, *631*, 8–16. [[CrossRef](#)]
17. Lu, Y.; Pei, C.; Han, X.; Li, Y.; Park, H.S.; Kim, J.K.; Yu, X. Tri-metallic fluoride nanoplates immobilized on reduced graphene architectures as efficient oxygen evolution reaction catalyst. *J. Electroanal. Chem.* **2024**, *957*, 118108. [[CrossRef](#)]
18. Pei, C.; Gu, Y.; Liu, Z.; Yu, X.; Feng, L. Fluoridated Iron–Nickel Layered Double Hydroxide for Enhanced Performance in the Oxygen Evolution Reaction. *ChemSusChem* **2019**, *12*, 3849–3855. [[CrossRef](#)] [[PubMed](#)]
19. Lin, L.; Piao, S.; Choi, Y.; Lyu, L.; Hong, H.; Kim, D.; Lee, J.; Zhang, W.; Piao, Y. Nanostructured Transition Metal Nitrides as Emerging Electrocatalysts for Water Electrolysis: Status and Challenges. *EnergyChem* **2022**, *4*, 100072. [[CrossRef](#)]
20. Zhang, H.; Wu, L.; Feng, R.; Wang, S.; Hsu, C.-S.; Ni, Y.; Ahmad, A.; Zhang, C.; Wu, H.; Chen, H.-M.; et al. Oxygen Vacancies Unfold the Catalytic Potential of NiFe-Layered Double Hydroxides by Promoting Their Electronic Transport for Oxygen Evolution Reaction. *ACS Catal.* **2023**, *13*, 6000–6012. [[CrossRef](#)]
21. Zhao, J.; Zhang, J.-J.; Li, Z.-Y.; Bu, X.-H. Recent Progress on NiFe-Based Electrocatalysts for the Oxygen Evolution Reaction. *Small* **2020**, *16*, 2003916. [[CrossRef](#)] [[PubMed](#)]
22. Xia, X.; Tu, J.; Zhang, Y.; Wang, X.; Gu, C.; Zhao, X.-B.; Fan, H.J. High-Quality Metal Oxide Core/Shell Nanowire Arrays on Conductive Substrates for Electrochemical Energy Storage. *ACS Nano* **2012**, *6*, 5531–5538. [[CrossRef](#)] [[PubMed](#)]
23. Zhao, L.; Cao, Q.; Wang, A.; Duan, J.; Zhou, W.; Sang, Y.; Liu, H. Iron oxide embedded titania nanowires—An active and stable electrocatalyst for oxygen evolution in acidic media. *Nano Energy* **2018**, *45*, 118–126. [[CrossRef](#)]
24. Wang, X.; Mao, Z.; Mao, X.; Hu, X.; Gao, F.; Gao, M.; Wu, Q.-L.; Lyu, X.; Du, A.; Xu, X.; et al. Dual Integrating Oxygen and Sulphur on Surface of CoTe Nanorods Triggers Enhanced Oxygen Evolution Reaction. *Adv. Sci.* **2023**, *10*, 2206204. [[CrossRef](#)] [[PubMed](#)]
25. Gu, X.; Yang, D.; Liu, Z.; Wang, S.; Feng, L. Iron oxide promoted nickel/nickel oxide rough nanorods for efficient urea assisted water splitting. *Electrochim. Acta* **2020**, *353*, 136516. [[CrossRef](#)]
26. Al-Naggar, A.H.; Shinde, N.M.; Kim, J.-S.; Mane, R.S. Water splitting performance of metal and non-metal-doped transition metal oxide electrocatalysts. *Coord. Chem. Rev.* **2023**, *474*, 214864. [[CrossRef](#)]
27. Silva, M.M.; Raimundo, R.A.; Silva, T.R.; Araújo, A.J.; Macedo, D.A.; Morales, M.A.; Souza, C.P.; Santos, A.G.; Lopes-Moriyama, A.L. Morphology-controlled NiFe₂O₄ nanostructures: Influence of calcination temperature on structural, magnetic and catalytic properties towards OER. *J. Electroanal. Chem.* **2023**, *933*, 117277. [[CrossRef](#)]
28. Li, L.; Cao, X.; Huo, J.; Qu, J.; Chen, W.; Liu, C.; Zhao, Y.; Liu, H.; Wang, G. High valence metals engineering strategies of Fe/Co/Ni-based catalysts for boosted OER electrocatalysis. *J. Energy Chem.* **2023**, *76*, 195–213. [[CrossRef](#)]
29. Gao, M.; Wang, L.; Yang, Y.; Sun, Y.; Zhao, X.; Wan, Y. Metal and Metal Oxide Supported on Ordered Mesoporous Carbon as Heterogeneous Catalysts. *ACS Catal.* **2023**, *13*, 4060–4090. [[CrossRef](#)]
30. Zhang, X.; Liu, Q.; Yan, Z.; Liu, S.; Wang, E. CuO/Co₃O₄ heterostructures with carbon nanotubes composites as ORR/OER electrocatalysts for Zn-air batteries. *J. Energy Storage* **2023**, *66*, 107485. [[CrossRef](#)]
31. He, H.; Lei, Y.; Liu, S.; Thummavichai, K.; Zhu, Y.; Wang, N. Tunable active-sites of Co– nanoparticles encapsulated in carbon nanofiber as high performance bifunctional OER/ORR electrocatalyst. *J. Colloid Interface Sci.* **2023**, *630*, 140–149. [[CrossRef](#)] [[PubMed](#)]
32. Park, J.W.; Park, G.; Kim, M.; Han, M.; Jang, J.; Yamauchi, Y.; Yuliarto, B.; Krüger, P.; Kim, J.; Park, N.; et al. Ni-single atom decorated mesoporous carbon electrocatalysts for hydrogen evolution reaction. *Chem. Eng. J.* **2023**, *468*, 143733. [[CrossRef](#)]
33. Yu, X.; Zhao, Z.; Pei, C. Surface oxidized iron-nickel nanorods anchoring on graphene architectures for oxygen evolution reaction. *Chin. Chem. Lett.* **2021**, *32*, 3579–3583. [[CrossRef](#)]
34. Chen, W.; Yu, X.; Zhao, Z.; Ji, S.; Feng, L. Hierarchical architecture of coupling graphene and 2D WS₂ for high-performance supercapacitor. *Electrochim. Acta* **2019**, *298*, 313–320. [[CrossRef](#)]
35. Chang, J.; Hu, Z.; Wu, D.; Xu, F.; Chen, C.; Jiang, K.; Gao, Z. Prussian blue analog-derived nickel iron phosphide-reduced graphene oxide hybrid as an efficient catalyst for overall water electrolysis. *J. Colloid Interface Sci.* **2023**, *638*, 801–812. [[CrossRef](#)] [[PubMed](#)]

36. Prabakaran, K.; Ingavale, S.B.; Kakade, B. Three dimensional NiS₂-Ni(OH)₂/CNT nanostructured assembly for supercapacitor and oxygen evolution reaction. *J. Alloys Compd.* **2020**, *812*, 152126. [[CrossRef](#)]
37. Zhao, J.-Y.; Wang, R.; Wang, S.; Lv, Y.-R.; Xu, H.; Zang, S.-Q. Metal-organic framework-derived Co₉S₈ embedded in N, O and S-tridoped carbon nanomaterials as an efficient oxygen bifunctional electrocatalyst. *J. Mater. Chem. A* **2019**, *7*, 7389–7395. [[CrossRef](#)]
38. Wang, Z.; Denis, D.K.; Zhao, Z.; Sun, X.; Zhang, J.; Hou, L.; Yuan, C. Unusual formation of hollow NiCoO₂ sub-microspheres by oxygen functional group dominated thermally induced mass relocation towards efficient lithium storage. *J. Mater. Chem. A* **2019**, *7*, 18109–18117. [[CrossRef](#)]
39. Wang, G.; Yang, J.; Park, J.; Gou, X.; Wang, B.; Liu, H.; Yao, J. Facile Synthesis and Characterization of Graphene Nanosheets. *J. Phys. Chem. C* **2008**, *112*, 8192–8195. [[CrossRef](#)]
40. Majumdar, A.; Dutta, P.; Sikdar, A.; Lee, H.; Ghosh, D.; Jha, S.N.; Tripathi, S.; Oh, Y.; Maiti, U.N. Impact of Atomic Rearrangement and Single Atom Stabilization on MoSe₂@NiCo₂Se₄ Heterostructure Catalyst for Efficient Overall Water Splitting. *Small* **2022**, *18*, 2200622. [[CrossRef](#)]
41. Zhou, G.; Ma, Y.; Gu, C.; Yang, J.; Pang, H.; Li, J.; Xu, L.; Tang, Y. Fe incorporation-induced electronic modification of Co-tannic acid complex nanoflowers for high-performance water oxidation. *Inorg. Chem. Front.* **2022**, *9*, 1091–1099. [[CrossRef](#)]
42. Chen, P.; Wang, T.; He, D.; Shi, T.; Chen, M.; Fang, K.; Lin, H.; Wang, J.; Wang, C.; Pang, H. Delocalized Isoelectronic Heterostructured FeCoOxSy Catalysts with Tunable Electron Density for Accelerated Sulfur Redox Kinetics in Li-S batteries. *Angew. Chem. Int. Ed.* **2023**, *62*, e202311693. [[CrossRef](#)] [[PubMed](#)]
43. Kapałka, A.; Fóti, G.; Comninellis, C. Determination of the Tafel slope for oxygen evolution on boron-doped diamond electrodes. *Electrochem. Commun.* **2008**, *10*, 607–610. [[CrossRef](#)]
44. Anantharaj, S.; Noda, S.; Driess, M.; Menezes, P.W. The Pitfalls of Using Potentiodynamic Polarization Curves for Tafel Analysis in Electrocatalytic Water Splitting. *ACS Energy Lett.* **2021**, *6*, 1607–1611. [[CrossRef](#)]
45. Zhang, H.; Guan, D.; Gu, Y.; Xu, H.; Wang, C.; Shao, Z.; Guo, Y. Tuning synergy between nickel and iron in Ruddlesden-Popper perovskites through controllable crystal dimensionalities towards enhanced oxygen-evolving activity and stability. *Carbon Energy* **2024**, e465. [[CrossRef](#)]

Disclaimer/Publisher's Note: The statements, opinions and data contained in all publications are solely those of the individual author(s) and contributor(s) and not of MDPI and/or the editor(s). MDPI and/or the editor(s) disclaim responsibility for any injury to people or property resulting from any ideas, methods, instructions or products referred to in the content.